RSC Advances




ROYAL SOCIETY OF CHEMISTRY

www.rsc.org/advances

## Table of contents

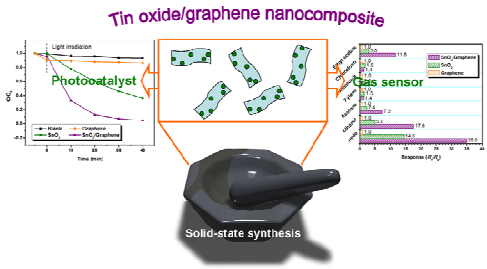


$SnO_2$/graphene nanocomposite with enhanced photocatalytic activity and gas sensing performance has been synthesized by solid-state chemical reaction in one-pot process.

Cite this: DOI: 10.1039/c0xx00000x

www.rsc.org/xxxxxx

ARTICLE TYPE

# Solid-state synthesis of $SnO_2$/graphene nanocomposite for photocatalysis and formaldehyde gas sensing

**Yali Cao,‡ Yizhao Li,‡ Dianzeng Jia* and Jing Xie**

***Received (in XXX, XXX) Xth XXXXXXXXX 20XX, Accepted Xth XXXXXXXXX 20XX***

**DOI: 10.1039/b000000x**

A facile solid-state synthetic route has been developed to prepare tin oxide-graphene ($SnO_2$/graphene) nanocomposite. Graphene decorated with tin oxide ($SnO_2$) nanoparticles was synthesized by *in situ* solid-state chemical reaction at room temperature. The obtained $SnO_2$/graphene nanocomposite has been investigated for applications as a photocatalyst to degrade organic contaminants in water and a chemical sensor to detect various vapours. The experiment results show that the $SnO_2$/graphene nanocomposite exhibited improved performances for photocatalytic decomposing of Methyl Orange and Rhodamine B, and formaldehyde sensing in comparison with the $SnO_2$ nanoparticles. The enhancement of properties is proposed to relate to the large specific surface area of nanocomposite and the good electronic characteristics of graphene.

## 1. Introduction

Metal oxide nanomaterials have potential applications in many fields, such as energy storage, water treatment, catalysis, sensors, etc.[1-5] Tin oxide ($SnO_2$), as an important n-type semiconductor, has attracted considerable interest due to its promising physical and chemical properties.[6-10] With a wide band gap of 3.6 eV and high thermal stability, nanostructured $SnO_2$ is generally considered as a strong candidate for photocatalysts and chemical sensors.[11-16] However, taking into account its practical applications, there are several fundamental issues must be considered and addressed. For example, the activity of $SnO_2$ nanoparticles with small size would decrease in the photocatalytic process because of the aggregation derived from their high surface energy. Its high electron-hole recombination rate is harmful to the efficiency of photocatalysis. The high work temperature and slow response time associated with the high activation energy of reaction also restrict their gas sensing applications. Therefore, many attempts have been made to improve the performances of nanostructured $SnO_2$.[17-24] Especially, $SnO_2$/graphene nanocoposites have been paid tremendous concerns owe to its enhanced electrical characteristics originated from the graphene.[25-31]

Some efforts have been made to fabricate $SnO_2$/graphene nanocoposites. Xue et al. have reported the synthesis of graphene-$SnO_2$ composite nanostructures through the electrophoretic deposition and magnetron sputtering techniques.[25] Honma et al. have fabricated $SnO_2$/graphene nanosheets composite by reassembled graphene nanosheets in the ethylene glycol solution in the presence of $SnO_2$ nanoparticles.[27] Some groups have developed a redox reaction between graphene oxide and $SnCl_2$ to prepare the $SnO_2$/graphene composites.[26, 28, 29, 32] The as-prepared samples in the literatures showed enhanced performances in the applications. However, the processes for the synthesis of $SnO_2$/graphene composites were complex, multi-step, and time-consuming. Therefore, it is essential to develop a simple route for the synthesis of $SnO_2$/graphene composites.

In this work, $SnO_2$/graphene composite was fabricated through a facile one-pot solid-state method. $SnO_2$ nanoparticles were *in situ* formed on the surface of graphene under ambient conditions. The photocatalytic and gas sensing properties of the resulting $SnO_2$/graphene composite were investigated. The incorporation of $SnO_2$ nanoparticles with graphene significantly improved the photocatalytic activity for degradation of Methyl Orange (MO) and Rhodamine B (RhB) in comparison with the $SnO_2$ nanoparticles. The $SnO_2$/graphene composite-based gas sensor also showed superior sensitivity and good selectivity to formaldehyde (HCHO). This method opens up a general route to prepare metal oxide/graphene nanocomposites with superior photocatalytic and gas sensing properties.

## 2. Experimental

### 2.1. Starting materials

All chemical were used as received without further purification. Tin(IV) chloride pentahydrate ($SnCl_4 \cdot 5H_2O$, 99.0%), sodium hydroxide (NaOH), and polyethylene glycol 400 (PEG-400) were purchased from Tianjin Guangfu Chemical Reagent Co., Ltd. Graphene (single layer, No. XF001) was obtained from Nanjing XFNANO Materials Tech Co., Ltd.

### 2.2. Synthesis

$SnO_2$/graphene nanocomposites were synthesized through a solid-state chemical reaction method. In a typical experiment, $SnCl_4 \cdot 5H_2O$ (0.70 g, 2 mmol), graphene (0.02 g, 3.0 wt% of tin salts), and PEG-400 (0.6 mL) were mixed by grinding in an agate

mortar at room temperature. Subsequently, NaOH (0.32 g, 8 mmol) was added into the mixtures and ground for 30 min. The reaction started readily during the addition of alkali, accompanied by emission of heat and evaporation of water vapor. The resulting solid products were washed with deionized water and absolute ethanol for several times. The products were then dried at 60°C for 12 h in air atmosphere.

For comparison, the same method was used to synthesize $SnO_2$ nanoparticles in the absence of graphene.

### 2.3. Characterization

Powder X-ray diffraction (XRD) patterns were recorded on a Bruker D8 X-ray diffractometer equipped with graphite-monochromatized Cu Kα radiation (λ = 1.54056 Å). Raman spectra were recorded on a Bruker Senterra Raman microscope. Field emission scanning electron microscope (FESEM) images were obtained on a Hitachi S-4800 scanning electron microscope with an accelerating voltage of 15 kV. Transmission electron microscope (TEM) and high resolution transmission electron microscope (HRTEM) images were obtained on a JEOL JEM-2010F electron microscope with an accelerating voltage of 200 kV. UV-vis spectra were obtained by a Hitachi U-3900H spectrophotometer. The Brunauer-Emmett-Teller (BET) and Barret-Joyner-Halender (BJH) results were measured on a Micromeritics ASAP 2020 surface area and porosity analyzer. Photoluminescence spectra were investigated on a Hitachi F-4500 spectrometer with an excitation wavelength of 250 nm.

### 2.4. Photocatalysis test

The photocatalytic activities of the samples were evaluated by the degradation of MO and RhB under UV irradiation using a 300 W mercury lamp. Typically, 20 mg of photocatalysts was added into 40 mL of 20 mg/L MO or RhB aqueous solution. The suspension was continuously stirred for 0.5 h in the dark to ensure the adsorption-desorption equilibrium between the photocatalysts and the MO or RhB. The solution was then shined under UV irradiation. At a given time, 3 mL of the suspension was collected and centrifuged to remove the photocatalysts then analyzed by the UV-vis spectra. All the experiments were conducted in a XPA-1 photochemical reactor (Nanjing Xujiang Electromechanical Plant) at room temperature.

### 2.5. Gas sensing test

Gas sensors were made in a conventional way.[33, 34] Briefly, the as-prepared products were dispersed in ethanol, which was used as the binder to form pastes. The alumina ceramic tube, assembled with platinum wire electrodes for electrical contacts, was dipped into the paste several times to form the sensing film. Then a Ni-Cr alloy wire as a resistance heater was passed through the ceramic tube. To improve the stability and repeatability, the sensors were aged at 300°C for 5 days in air prior to use. The test was carried out in a commercial gas sensing measurement system of WS-30A (Zhengzhou Winsen Electronic Technology Co., Ltd.).

Response of a sensor was defined as follows:

Response = $R_a$ / $R_g$

$R_a$ is the resistance of the sensor in air, and $R_g$ is that in a mixture of testing gases and air.

## 3. Results and discussion

### 3.1. Structure and morphology characterization

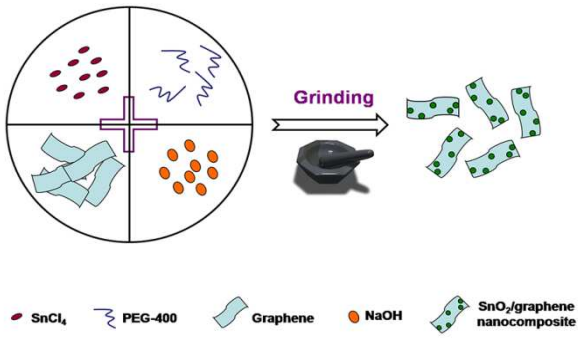


**Scheme 1** Schematic illustration of the fabrication of the $SnO_2$/graphene nanocomposite.

The $SnO_2$/graphene nanocomposite was synthesized by grinding the reactants in one-pot process at ambient conditions. A schematic pattern for the formation process of the $SnO_2$/graphene nanocomposite is shown in Scheme 1. In the solid-state synthesis, $SnO_2$ nanoparticles firstly nucleate and form in the presence of PEG-400 through the reaction of $SnCl_4$ and NaOH. Then, $SnO_2$ nanoparticles supported on graphene composite is obtained by van der Waals interaction between the $SnO_2$ nanoparticles and graphene. This solid-state chemical reaction route of preparing $SnO_2$/graphene nanocomposite is very suitable for large-scale synthesis, and has great potential in practical applications.

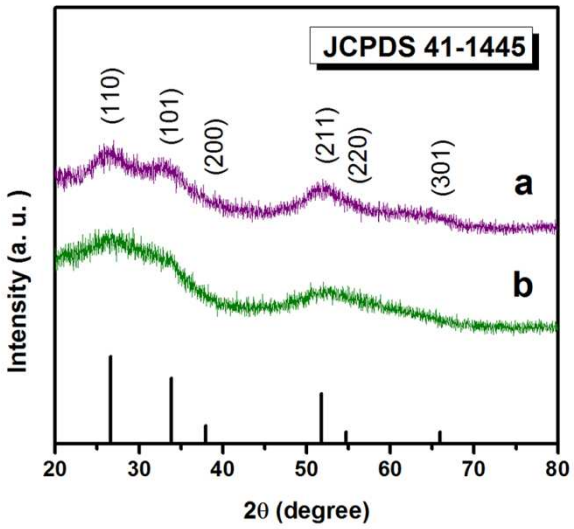


**Fig. 1** XRD patterns of (a) the nanocomposite and (b) the nanoparticles.

The XRD patterns of the as-prepared $SnO_2$/graphene nanocomposite and $SnO_2$ nanoparticles are shown in Fig. 1. All peaks can be indexed to $SnO_2$ with the tetragonal cassiterite structure (JCPDS No. 41-1445). The broader diffraction peaks suggest the fine grain size of the products. However, no obvious peaks from graphene are observed in Fig. 1a, indicating that the $SnO_2$ nanoparticles deposited on graphene sheets can prevent them from stacking into multilayers.[35, 36]

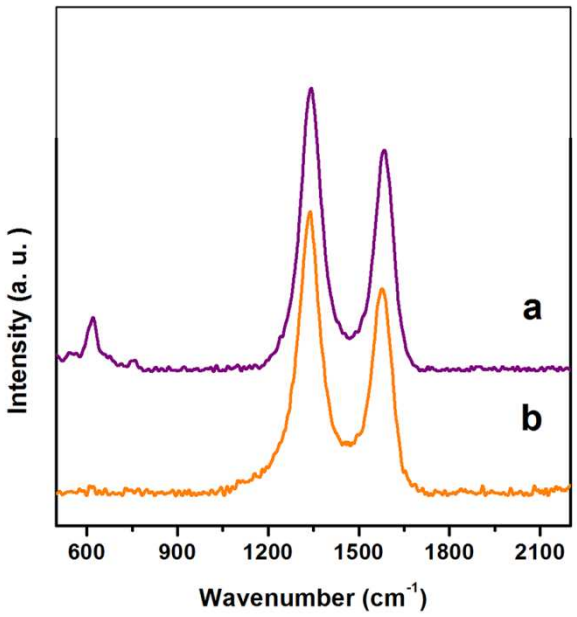


**Fig. 2** Raman spectra of (a) the $SnO_2$/graphene nanocomposite and (b) the graphene.

Raman studies were carried out to confirm the presence of graphene on the composites. It can be clearly seen that there are two broad peaks at around 1341 and 1580 $cm^{-1}$ in both of $SnO_2$/graphene nanocomposite and graphene from Fig. 2, corresponding to the D and G bands of graphene, respectively. The intensity ratio (1.28) of D over G band ($I_D/I_G$) of the nanocomposite is lower than that of graphene (1.37), which is regarded as the interaction between the $SnO_2$ nanoparticles and the graphene sheets in the $SnO_2$/graphene nanocomposite.[37] In addition, for the $SnO_2$/graphene nanocomposite, there is an additional peak at around 620 $cm^{-1}$, which is attributed to the $A_{1g}$ vibration mode of $SnO_2$.[38, 39]

To investigate the morphology of the products, FESEM, TEM, and HRTEM images were taken for the graphene, $SnO_2$ nanoparticles, and $SnO_2$/graphene nanocomposite. Fig. 3a presents the representative FESEM image of the graphene. It shows clear two dimensional (2D) structure of the thin layers. As shown in Fig. 3b, the FESEM image of the $SnO_2$ nanoparticles exhibits spherical particles with the size of 50-200 nm. In the FESEM image of the composite in Fig. 3c, it can be seen that 2D graphene sheets are decorated by numerous particles. More-detailed structural information of the products was provided by TEM and HRTEM images. Fig. 3d shows that the as-prepared $SnO_2$ sample is composed of many small particles. The inset of Fig. 3d clearly shows that the size of crystalline grain is about 2-3 nm. In Fig. 3e, the TEM and HRTEM images of the composite show that $SnO_2$ nanoparticles are supported uniformly on the graphene sheets.

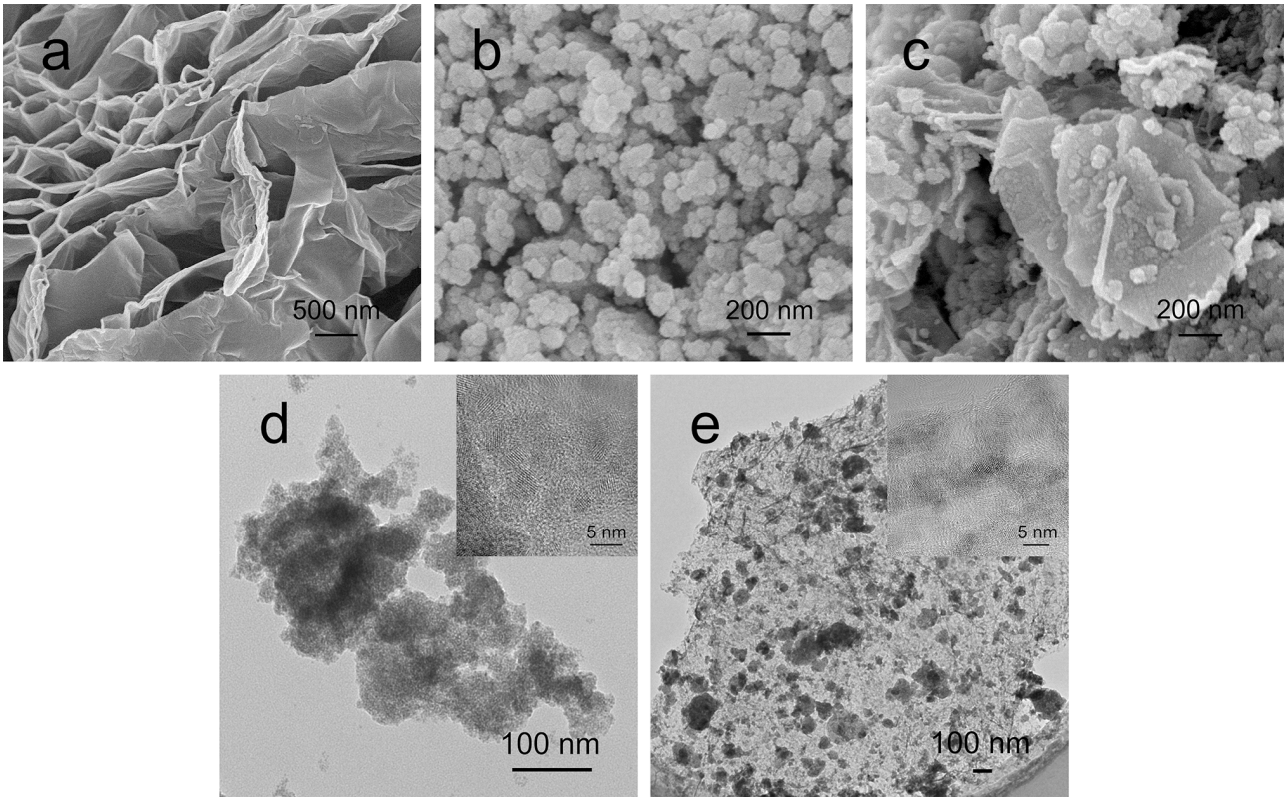


**Fig. 3** Typical FESEM images of (a) the graphene, (b) the $SnO_2$ nanoparticles, and (c) the $SnO_2$/graphene nanocomposite; typical TEM images of (d) the $SnO_2$ nanoparticles and (e) the $SnO_2$/graphene nanocomposite, the insets are the corresponding HRTEM images.

### 3.2. Photocatalytic properties and mechanism

Cite this: DOI: 10.1039/c0xx00000x

www.rsc.org/xxxxxx

# ARTICLE TYPE

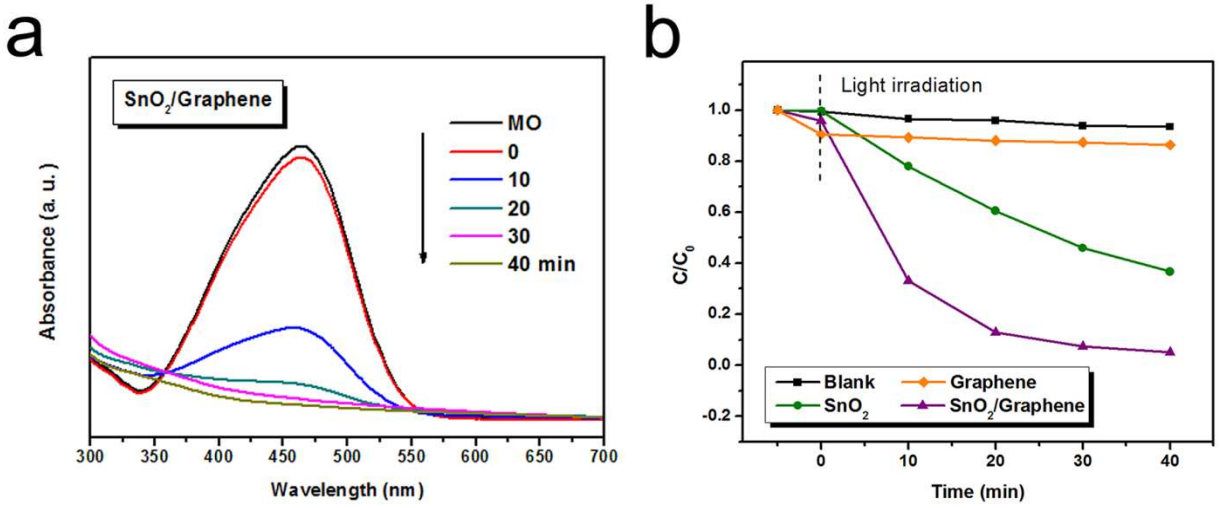


**Fig. 4** (a) UV-vis absorption spectra of MO at different times in the presence of the $SnO_2$/graphene nanocomposite; (b) plot of relative concentration of residual MO versus time under UV irradiation.

The photocatalytic degradation of organic dyes is of great significance in environmental pollutant treatment. The as-prepared samples were firstly investigated as photocatalysts to degrade MO, which is a typical anionic dye, under UV irradiation. Fig. 4a presents the UV-vis absorption spectra of the aqueous MO solution using $SnO_2$/graphene nanocomposite in various durations. The characteristic absorbance at 465 nm of MO in aqueous solution quickly decreases with the time of UV irradiation, which indicates that MO was gradually degraded in the presence of nanocomposite under UV irradiation. As seen in Fig. 4b, 95% of MO is degraded within 40 min when using nanocomposite as phtocatalyst, whereas only 63% of MO is degraded with $SnO_2$ nanoparticles in the same period. In addition, the decomposition of MO is inappreciable in the presence of graphene and in the absence of phtocatalysts within the test period, suggesting that photolysis of MO is negligible and photocatalysts play a key role in the degradation of MO.

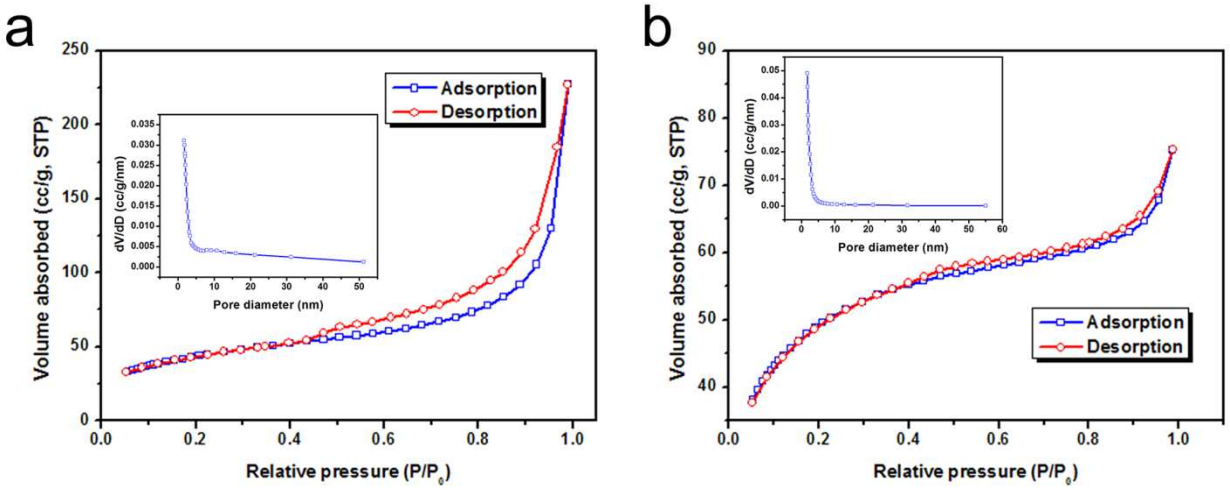


**Fig. 5** Nitrogen adsorption-desorption isotherms of (a) the $SnO_2$/graphene nanocomposite and the inset is the corresponding pore size distribution; (b) the $SnO_2$ nanoparticles and the inset is the corresponding pore size distribution.

The high specific surface area of photocatalysts is helpful for the increase of photocatalytic activity. Fig. 5 shows nitrogen adsorption-desorption isotherms and the corresponding pore size distributions of the photocatalysts. The specific surface area and the total pore volume of $SnO_2$/graphene nanocomposite are 156.8 $m^2/g$ and 0.35 $cm^3/g$, which are higher than that of $SnO_2$

nanoparticles (143.3 $m^2/g$ and 0.11 $cm^3/g$), respectively. The large specific surface area of nanocomposite is beneficial to absorb more light and increase the number of unsaturated surface coordination sites resulting in improvement of photocatalytic performance.[40]

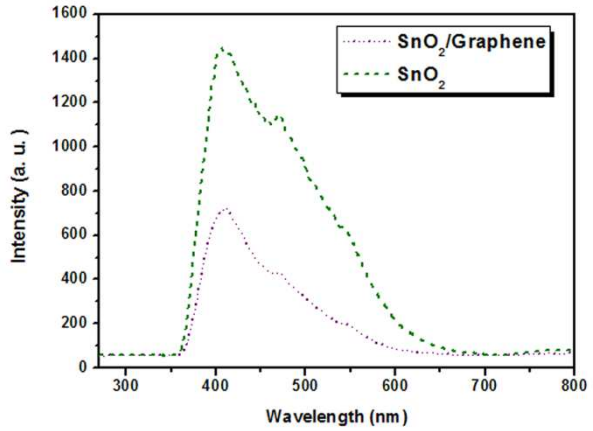


**Fig. 6** PL spectra of the $SnO_2$/graphene nanocomposite and the $SnO_2$ nanoparticles.

It is well-known that the inhibiting recombination of photogenerated electron-hole pair can greatly enhance the efficiency of photocatalysis.[41-43] The introduction of graphene is expected to influence the path of charge transfer and, hence, to improve the photocatalytic activity of nanocomposite. The PL spectra of $SnO_2$ nanoparticles and $SnO_2$/graphene nanocomposite excited at 250 nm are given in Fig. 6. The $SnO_2$ nanoparticles show a strong PL emission band at 406 nm. After combined with graphene, the PL intensity of $SnO_2$/graphene nanocomposite greatly decreases, which suggests the number of the emitted electrons resulting from the recombination between excited electrons and holes decreases accordingly.[44] Therefore, the nanocomposite shows the improved performance in photocatalysis.

In the photocatalytic process, more electron-hole pairs can be generated in the $SnO_2$/graphene nanocomposite because of its large specific surface area. The hole in $SnO_2$ can take part in the redox reactions, and the electron can transfer from the conduction band of $SnO_2$ to graphene and then react with the absorbed $O_2$ to form ·OH for the further photocatalytic degradation of MO. The effective charge transfer can reduce the electron-hole pair recombination and increase the photocatalytic activity of $SnO_2$/graphene nanocomposite.

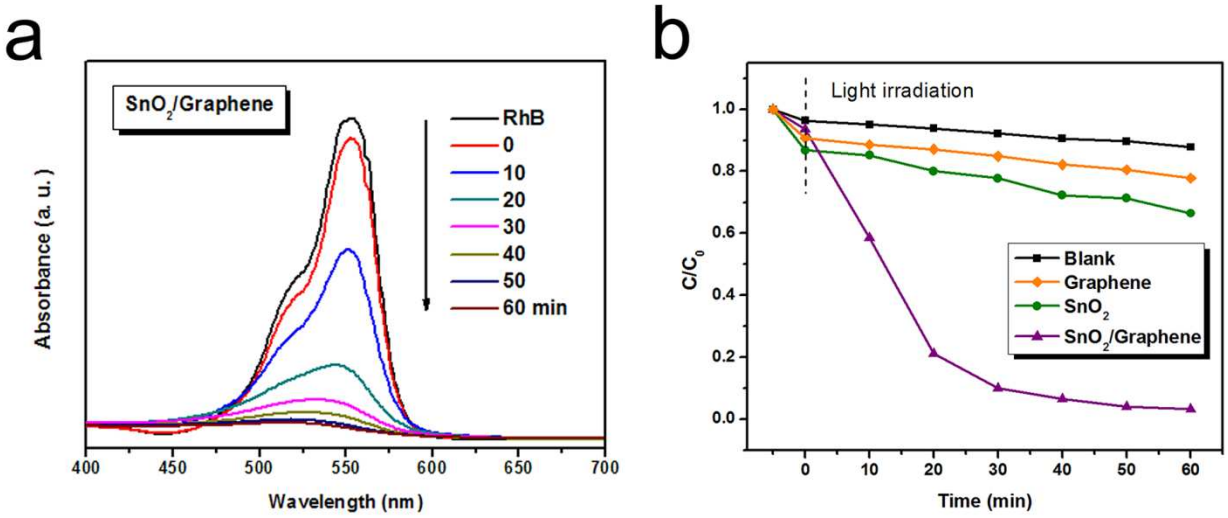


**Fig. 7** (a) UV-vis absorption spectra of RhB at different times in the presence of the $SnO_2$/graphene nanocomposite; (b) plot of relative concentration of residual RhB versus time under UV irradiation.

To confirm the versatility of the photocatalysts, the experiments for the degradation of RhB, which is a typical cationic dye, with the obtained samples were also conducted. As shown in Fig. 7a, the absorption band at 554 nm decreases rapidly as the irradiation time prolonging, when the $SnO_2$/graphene nanocomposite is used as photocatalyst. It can be found from Fig. 7b that 97% of RhB is degraded with $SnO_2$/graphene composite after exposure under UV irradiation for 60 min. As for $SnO_2$ nanoparticles, only 34% of RhB is degraded within the same time. The results undoubtedly demonstrate that the $SnO_2$/graphene nanocomposite have superior photocatalytic activity compared with $SnO_2$ nanoparticles. It is worth noting that the degradations of different kinds of dyes are achieved in the present study, which suggests the versatility of the $SnO_2$/graphene nanocomposite for photocatalysis application.

### 3.3. Gas sensing properties

Cite this: DOI: 10.1039/c0xx00000x

www.rsc.org/xxxxxx

# ARTICLE TYPE

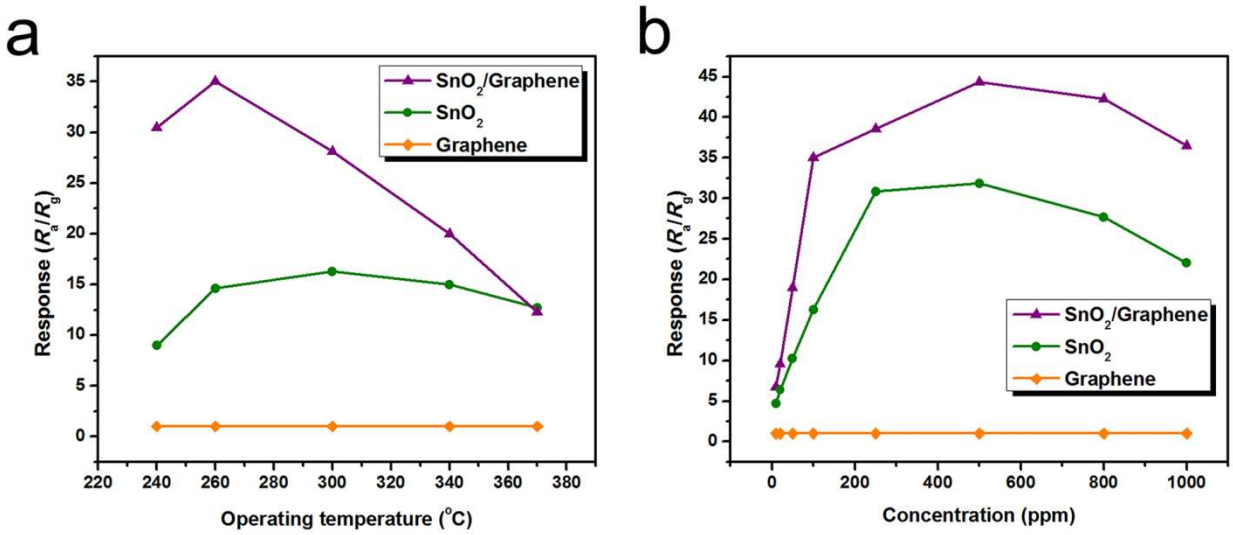


**Fig. 8** (a) Relationship of the working temperature versus response of the sensors to 100 ppm HCHO; (b) relationship between the response and the concentration of HCHO.

HCHO is one of the main sources for house pollution and is harmful for people. It is significant to effectively detect and monitor HCHO using a suitable sensor.[45-47] Thus, the gas sensing properties of as-prepared samples have also been investigated. Fig. 8a shows the response values of the sensors based on graphene, $SnO_2$ nanoparticles, and $SnO_2$/graphene nanocomposite to 100 ppm HCHO at different operating temperatures, respectively. It can be observed that graphene does not respond to HCHO. The maximum sensitivity of the nanocomposite is 35.0 at 260°C. It is superior to other $SnO_2$-based formaldehyde gas sensor reported in the literature.[48-50] For the $SnO_2$ nanoparticles, the highest response is only 16.3 at 300°C. It can be seen that the $SnO_2$/graphene nanocomposite has a greater sensitivity and a lower working temperature than the $SnO_2$ nanoparticles. Fig. 8b shows the correlation between the concentrations and the responses to HCHO vapor of sensors based on the nanocomposite and nanoparticles. These measurements were conducted by injecting specific amounts of the testing liquid into the testing chamber at the optimal operating temperatures of the sensors. For nanocomposite and $SnO_2$ nanoparticles, the response values firstly increase with increasing the gas concentrations. Then the responses of the sensors decrease after reaching the maximum. The responses to 500 ppm HCHO of the $SnO_2$/graphene and $SnO_2$ are 44.3 and 31.8 at operating temperatures of 260°C and 300°C, respectively. The high specific surface area and large pore volume of the $SnO_2$/graphene nanocomposite are of great benefit to the adsorption and diffusion of gas molecules.[51, 52] Therefore, the sensor based on the nanocomposite exhibits the improved sensitivity in detecting HCHO.

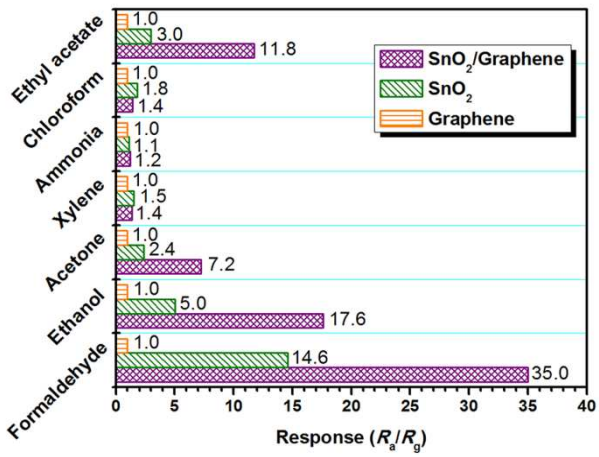


**Fig. 9** Responses of the sensors to 100 ppm various vapours at 260°C.

The selectivity is the important parameter of gas sensors for the practical application. Fig. 9 shows the responses of the sensors to the various organic vapours, such as HCHO, ethanol, acetone, xylene, ammonia, chloroform, ethyl acetate, with the concentration of 100 ppm at 260°C. The nanocomposite-based sensor shows relatively lower responses to the interferential gases than to the HCHO. It suggests that the $SnO_2$/graphene nanocomposite have a good selectivity to the target vapour. In addition, the resistance transients of the sensor have been shown in Supplementary Information, which further validates the results.

## 4. Conclusions

In summary, the $SnO_2$/graphene nanocomposite was prepared by a facile solid-state chemical reaction at room temperature. It was found that the $SnO_2$/graphene nanocomposite possessed the improved photocatalytic properties for the degradation of MO and RhB. The nanocomposite-based gas sensor also exhibited superior sensitivity and good selectivity to HCHO vapour. The large specific surface area and good electronic characteristics are responsible for the enhancement of properties of the nanocomposite. The favourable results suggest that the $SnO_2$/graphene nanocomposite synthesized by the solid-state route is a promising candidate for high performance photocatalyst and gas sensor.

## Acknowledgement

This work was financially supported by China Postdoctoral Science Foundation (no. 2014T70955), Excellent Postdoctoral Ordinary Funded Projects of the Xinjiang Uygur Autonomous Region, the Doctoral Innovation Program of Xinjiang University (no. XJUBSCX-2012019), Graduate Research Innovation Project of Xinjiang (no. XJGRI2013020), National Natural Science Foundation of China (nos. 21101132, 21271151, 21361024 and U1203292).

## Notes and references

*Key Laboratory of Material and Technology for Clean Energy, Ministry of Education, Key Laboratory of Advanced Functional Materials, Autonomous Region, Institute of Applied Chemistry, Xinjiang University, Urumqi, Xinjiang 830046, China. Fax: +86 991 8580032; Tel: +86 991 8583083; E-mail: jdz@xju.edu.cn*

† Electronic Supplementary Information (ESI) available: the resistance transients of the sensors. See DOI: 10.1039/b000000x/

‡ These authors contributed equally to this work.

1. A. S. Arico, P. Bruce, B. Scrosati, J. M. Tarascon and W. van Schalkwijk, *Nat. Mater.*, 2005, **4**, 366-377.
2. M. E. Franke, T. J. Koplin and U. Simon, *Small*, 2006, **2**, 36-50.
3. N. A. Frey, S. Peng, K. Cheng and S. Sun, *Chem. Soc. Rev.*, 2009, **38**, 2532-2542.
4. L. S. Zhong, J. S. Hu, H. P. Liang, A. M. Cao, W. G. Song and L. J. Wan, *Adv. Mater.*, 2006, **18**, 2426-2431.
5. L. S. Zhong, J. S. Hu, A. M. Cao, Q. Liu, W. G. Song and L. J. Wan, *Chem. Mater.*, 2007, **19**, 1648-1655.
6. Z. R. Dai, J. L. Gole, J. D. Stout and Z. L. Wang, *J. Phys. Chem. B*, 2002, **106**, 1274-1279.
7. C. Kim, M. Noh, M. Choi, J. Cho and B. Park, *Chem. Mater.*, 2005, **17**, 3297-3301.
8. A. Kolmakov, Y. Zhang, G. Cheng and M. Moskovits, *Adv. Mater.*, 2003, **15**, 997-1000.
9. F. Zhang, K. X. Wang, X. Y. Wang, G. D. Li and J. S. Chen, *Dalton Trans.*, 2011, **40**, 8517-8519.
10. X. Wang, S. Qiu, J. Liu, C. He, G. Lu and W. Liu, *Eur. J. Inorg. Chem.*, 2014, 863-869.
11. H. C. Chiu and C. S. Yeh, *J. Phys. Chem. C*, 2007, **111**, 7256-7259.
12. Y. Han, X. Wu, Y. Ma, L. Gong, F. Qu and H. Fan, *CrystEngComm*, 2011, **13**, 3506-3510.
13. X. W. Lou, Y. Wang, C. Yuan, J. Y. Lee and L. A. Archer, *Adv. Mater.*, 2006, **18**, 2325-2329.
14. Y. Wang, X. Jiang and Y. Xia, *J. Am. Chem. Soc.*, 2003, **125**, 16176-16177.
15. S. Wu, H. Cao, S. Yin, X. Liu and X. Zhang, *J. Phys. Chem. C*, 2009, **113**, 17893-17898.
16. Q. Zhao, Y. Gao, X. Bai, C. Wu and Y. Xie, *Eur. J. Inorg. Chem.*, 2006, 1643-1648.
17. Y. Chen, C. Zhu and T. Wang, *Nanotechnology*, 2006, **17**, 3012.
18. S. W. Choi, J. Y. Park and S. S. Kim, *Nanotechnology*, 2009, **20**, 465603.
19. T. Jia, W. Wang, F. Long, Z. Fu, H. Wang and Q. Zhang, *J. Phys. Chem. C*, 2009, **113**, 9071-9077.
20. M. Niu, F. Huang, L. Cui, P. Huang, Y. Yu and Y. Wang, *ACS Nano*, 2010, **4**, 681-688.
21. W. W. Wang, Y. J. Zhu and L. X. Yang, *Adv. Funct. Mater.*, 2007, **17**, 59-64.
22. S. Balachandran, K. Selvam, B. Babu and M. Swaminathan, *Dalton Trans.*, 2013, **42**, 16365-16374.
23. Y. Jia, P. Y. Wu, Y. P. Jiang, Q. Y. Zhang, S. S. Zhou, F. Fang and D. Y. Peng, *New J. Chem.*, 2014, **38**, 1100-1105.
24. J. W. Yoon, Y. J. Hong, Y. Chan Kang and J. H. Lee, *RSC Adv.*, 2014, **4**, 16067-16074.
25. J. Ding, X. Yan, J. Li, B. Shen, J. Yang, J. Chen and Q. Xue, *ACS Appl. Mater. Interfaces*, 2011, **3**, 4299-4305.
26. Q. Lin, Y. Li and M. Yang, *Sens. Actuators, B*, 2012, **173**, 139-147.
27. S. M. Paek, E. Yoo and I. Honma, *Nano Lett.*, 2008, **9**, 72-75.
28. H. Seema, K. C. Kemp, V. Chandra and K. S. Kim, *Nanotechnology*, 2012, **23**, 355705.
29. H. Song, L. Zhang, C. He, Y. Qu, Y. Tian and Y. Lv, *J. Mater. Chem.*, 2011, **21**, 5972-5977.
30. H. Seema, K. C. Kemp, V. Chandra and K. S. Kim, *Nanotechnology*, 2012, **23**, 355705.
31. Y. Zhu, C. Li and C. Cao, *RSC Adv.*, 2013, **3**, 11860-11868.
32. Y. Li, X. Lv, J. Lu and J. Li, *J. Phys. Chem. C*, 2010, **114**, 21770-21774.
33. Y. Cao, W. Pan, Y. Zong and D. Jia, *Sens. Actuators, B*, 2009, **138**, 480-484.
34. Y. Zong, Y. Cao, D. Jia and P. Hu, *Sens. Actuators, B*, 2010, **145**, 84-88.
35. P. Lian, S. Liang, X. Zhu, W. Yang and H. Wang, *Electrochim. Acta*, 2011, **58**, 81-88.
36. L. S. Zhang, L. Y. Jiang, H. J. Yan, W. D. Wang, W. Wang, W. G. Song, Y. G. Guo and L. J. Wan, *J. Mater. Chem.*, 2010, **20**, 5462-5467.
37. B. Li and H. Cao, *J. Mater. Chem.*, 2011, **21**, 3346-3349.
38. J. Q. Hu, X. L. Ma, N. G. Shang, Z. Y. Xie, N. B. Wong, C. S. Lee and S. T. Lee, *J. Phys. Chem. B*, 2002, **106**, 3823-3826.
39. K. N. Yu, Y. Xiong, Y. Liu and C. Xiong, *Phys. Rev. B*, 1997, **55**, 2666-2671.
40. F. J. Chen, Y. L. Cao and D. Z. Jia, *CrystEngComm*, 2013, **15**, 4747-4754.
41. J. Lee, H. S. Shim, M. Lee, J. K. Song and D. Lee, *J. Phys. Chem. Lett.*, 2011, **2**, 2840-2845.
42. Y. Li, G. Chen, Q. Wang, X. Wang, A. Zhou and Z. Shen, *Adv. Funct. Mater.*, 2010, **20**, 3390-3398.
43. W. Yang, L. Zhang, Y. Hu, Y. Zhong, H. B. Wu and X. W. Lou, *Angew. Chem. Int. Ed.*, 2012, **51**, 11501-11504.
44. J. Kim, J. S. Lee and M. Kang, *Bull. Korean Chem. Soc.*, 2011, **32**, 1715-1720.
45. Y. Cao, P. Hu, W. Pan, Y. Huang and D. Jia, *Sens. Actuators, B*, 2008, **134**, 462-466.
46. Z. Wang, J. Liu, F. Wang, S. Chen, H. Luo and X. Yu, *J. Phys. Chem. C*, 2010, **114**, 13577-13582.
47. J. Xu, X. Jia, X. Lou, G. Xi, J. Han and Q. Gao, *Sens. Actuators, B*, 2007, **120**, 694-699.
48. Z. Li, Q. Zhao, W. Fan and J. Zhan, *Nanoscale*, 2011, **3**, 1646-1652.
49. J. Wang, L. Liu, S. Y. Cong, J. Q. Qi and B. K. Xu, *Sens. Actuators, B*, 2008, **134**, 1010-1015.
50. Y. Zheng, J. Wang and P. Yao, *Sens. Actuators, B*, 2011, **156**, 723-730.
51. J. H. Lee, *Sens. Actuators, B*, 2009, **140**, 319-336.
52. G. J. Li, X. H. Zhang and S. Kawi, *Sens. Actuators, B.*, 1999, **60**, 64-70.